Version of Record: https://www.sciencedirect.com/science/article/pii/S0378775321003050
Manuscript_2b692e5d03f7d2e74da81e74caed4814

Layer-Structured Triple-Conducting Electrocatalyst for Water-Splitting in Protonic Ceramic Electrolysis Cells: Conductivities vs. Activity

Wenyuan Li[a], Bo Guan[a], Tao Yang[b,c], Zhongqiu Li[a,d], Wangying Shi[a], Hanchen Tian[a], Liang Ma[a,e], Thomas L. Kalapos[b,c], Xingbo Liu[a,*]

[a]Mechanical & Aerospace Engineering Department, Benjamin M. Statler College of Engineering & Mineral Resources, West Virginia University, Morgantown, WV 26506, USA

[b]National Energy Technology Laboratory, Morgantown, WV 26505, USA

[c]Leidos Research Support Team, Morgantown WV, 26506, USA

[d]School of Physics & Electronic Engineering, Harbin Normal University, Harbin, 150025, China

[e]School of Materials Science and Engineering, Hebei University of Engineering, Handan, 056038, China

Abstract

Electron, proton and oxygen-triple-conducting materials are becoming the dominant steam electrode candidate to break the rate limit on the water-splitting reaction that throttles the performance of protonic ceramic electrolysis cells (PCECs). In this study, based on $Pr_2NiO_{4+\delta}$ Ruddlesden-Popper phase, we manipulate these conductivities by Pr-site Ba substitution to probe the correlation of each conductivity with the kinetics of the elementary reaction steps. It is found that the proton conductivity is vital to sustain an extended active surface area for faster adsorption of reactants and desorption of products. The effect of oxygen conductivity is surprisingly found insignificant in the water-splitting reaction. On the contrary, surface oxygen removal is discovered as the most rate-limiting process. The electronic conductivity is not a direct limiting factor. However, an electron transfer process between

* Corresponding author, E-mail address: Xingbo.liu@mail.wvu.edu

© 2021 published by Elsevier. This manuscript is made available under the Elsevier user license
https://www.elsevier.com/open-access/userlicense/1.0/

the current collector and the electrode junction could introduce extra resistance that is perceptible at a high operating temperature range. The best water-splitting activity is obtained on a proton conductivity/oxygen surface desorption capability well-balanced sample after Ba substitution. As a result, a water-splitting reaction resistance of 0.022 Ωcm^2, a current density of 1.96 A/cm^2 at 700°C is achieved on $Pr_{1.7}Ba_{0.3}NiO_{4+\delta}$, one of the best performances for PCECs.

1. Introduction

To realize environmentally sustainable development, a worldwide effort has been paid to phase out fossil fuel and establish a so-called "hydrogen economy". In this hydrogen economy, H_2 will be used for transportation, household heating, power generation, energy storage, and long-distance transport of energy. It provides a much cleaner and cost-effective solution to keep the ball of economy growing, and is deemed as the building block of the future's low-carbon ecosystem.[1] However, more than 90% of global H_2 production to date is still fossil energy-based, rendering the utilization of this carbon-flavored H_2 product less attractive. On the other hand, water electrolysis using electricity from renewable energy sources represents a zero-carbon strategy for H_2 production.[2, 3] Among various types of electrolysis, PCECs have been attracting focused attention from investigators due to their enormous promise for high-efficient operation and large-scale deployment.[4-8] PCEC operates at 500-700°C, able to use heat as energy input to reduce the use of electricity, providing much fast H_2 production kinetics than the low-temperature alkaline water electrolysis or polymer electrolyte membrane electrolysis.[9, 10] There is no need to elevate the operating temperature to 750~850°C for fast H_2 generation, which would otherwise pose challenging requirements of materials, maintenance, and service lifespan to the system. Recently, significant progress has been made in PCECs in terms of advanced materials,[11-15] innovative structures,[16-18] and rational system designs.[19] Regarding the critical performance feature of the PCECs, it is generally acknowledged that the kinetics of the

steam electrode needs to be substantially enhanced to match that of the Ni-based fuel electrode for a well-balanced, highly efficient PCEC.[7] Starting 2012,[20] a new vision comes into shape that electron, proton, and oxygen-triple-conducting materials may be developed for PCECs to replace the traditional mixed ionic (i.e. oxygen) and electronic conductive (MIEC) electrode that is borrowed from the oxygen-conducting solid oxide cells.[21] It is aimed to disruptively promote the electrolysis performance by upgrading the one dimensional, three-phase boundary (3PB)-associated reactive pathway in the traditional MIEC electrodes to a three-dimensional, two-phase boundary (2PB)-associated, particularly active network in the new triple-conducting electrode via their multiple conducting ability.

Lately, several triple-conducting materials have been found as excellent steam electrodes for PCECSs. Duan et al.[22] reported a 1.1 A/cm^2 electrolysis current at 1.3V 600ºC for a PCEC with $BaCo_{0.4}Fe_{0.4}Zr_{0.1}Y_{0.1}O_{3-\delta}$ steam electrode. Ding et al.[23] achieved a 1.2 A/cm^2 electrolysis current at 1.3 V 600°C on a PCEC with $PrNi_{0.5}Co_{0.5}O_{3-\delta}$ steam electrode. Choi et al.[18] reported a 1.8A/cm^2 performance for a PCEC with PLD modified $PrBa_{0.5}Sr_{0.5}Co_{1.5}Fe_{0.5}O_{5+\delta}$ steam electrode. Other outstanding materials include $(PrBa_{0.8}Ca_{0.2})_{0.95}Co_2O_{6-\delta}$ reported by Tang et al.[24], $Sr_2Fe_{1.5}Mo_{0.5}O_{6-\delta}$ by Lei et al.,[12] $Sr_{2.8}La_{0.2}Fe_2O_{7-\delta}$ by Huan et al,[13] etc. Of those newly emerged candidates, one prominent example is the Ruddlesden-Popper (RP) phase species.[11, 16, 25] This unique layer-structured RP phase consists of an ABO_3 perovskite layer stacking alternatively with an AO rock salt layer. It shows good electronic and oxygen conductivities. The open channel in the AO layer could possibly allow easy water insertion. Proton conduction has been proven on this structure.[20] These featured properties make the RP phase attractive to conduct chemical tuning for performance breakthrough and to dig into the fundamental question of how these triple conductivities interplay to affect the water-splitting kinetics in this new application scenario. In this study, we investigate a new

RP phase series, $Pr_{2-x}Ba_xNiO_{4+\delta}$. Ba^{2+} is a Lewis acid and H_2O is a Lewis base. The addition of Ba to A-site could benefit the steam adsorption process. Meanwhile, aliovalent Ba^2 substitution for Pr^{4+} can adjust the electron, oxygen, and proton conductivities, which is used to clarify the role of each conductivity in the overall water-splitting reaction, and to guide the future materials design toward high performance and stability electrodes in the protonic ceramic electrolysis cells.

2. Experimental

2.1 Materials synthesis and chemical properties

RP phase steam electrode materials $Pr_{2-x}Ba_xNiO_{4+\delta}$ (PBN, and specifically designated as PNO for x=0, PB10, 20, 30, 40 and 50 for x=0.1, 0.2, 0.3, 0.4 and 0.5) and $BaZr_{0.1}Ce_{0.7}Y_{0.1}Yb_{0.1}O_{3-\delta}$ (BZCYYb) electrolyte powders were synthesized by ethylenediaminetetraacetic (EDTA)-citric sol-gel method.[26-28] During synthesis, citric acid together with stoichiometric nitrates were first dissolved into distilled water. EDTA as complexing agent was dissolved into diluted ammonia water. The mole ratio of metal cation:citric acid:EDTA was set to 1:1.5:1. The nitrate and EDTA solutions were then mixed together, followed by adjusting pH value to 8~10 using ammonia water or nitric acid. Afterward, the solution was held at ~80ºC and stirred until gelation on a magnetic heating plate. The gel was heated at 600ºC in air to decompose nitrates and residual organics. The resultant PBN powders were calcined in air at 1200ºC for 4 h, BZCYYb powder in air at 1150ºC for 10 h. Calcined powders were ball-milled in a planetary miller for 12 h. The phase purity was examined by X-ray diffraction (XRD, PANalytical X'pert PRO, Cu Kα radiation). To verify the chemical compatibility between PBN and BZCYYb, each composition was thoroughly mixed with electrolyte at a 1:1 wt. ratio in a mortar and calcined at 1150ºC for 3h. To verify the chemical stability of PBN towards steam, PBN powders were exposed to flowing 60 vol.% water vapor-containing air at 700ºC for 12h. XRD was conducted to examine structural change after these treatments.

2.2 Fabrication of samples

Dense bar samples were prepared for conductivity-related measurement. 2.5 g PBN powders were pressed to a pellet in a 16 mm die at 300 MPa. The pellets were sintered at 1300°C in air 4h for densification. The relative density was determined through the Archimedes method combined with XRD lattice parameters (96%, 93%, 95%, 93%, 92% for PNO, PB10, PB20, PB30 and PB40). Bar samples were cut from the pellets through a diamond saw and polished by sandpapers and 1μm Al_2O_3 polishing paste. Two gold wires were attached to each end by gold paste as lead wire. DC electrical conductivity in air, and electrical conductivity relaxations in relevant atmospheres were measured through these dense bar samples.

To make half cells for steam electrode characterization, mixed electrode/BZCYYb electrolyte powders (1:1 wt. ratio) were blended in an ink vehicle (Fuel Cell Materials Co.) (powders:vehicle=5:4 wt.), then ground in a mortar until homogeneous anode slurry was formed. To make electrolyte pellets, a proportional amount of $Zn(NO_3)_2$ ethanol solution was added to BZCYYb powders at a ZnO (sintering aid):BZCYYb=1:100 wt ratio, then dried at 220°C overnight. The electrolyte powders were pressed to pellets in a similar way as PBN pellet and sintered in air at 1300°C 4h for densification. Composite PBN-BZCYYb anode slurry was symmetrically screen-printed to the BZCYYb electrolyte with an area of 0.5 cm^2, followed by sintering at 1150°C for 3 h.

Full cells were fabricated with a NiO-BZCYYb cathode-supported structure. Cathode powders of NiO:BZCYYb:flour (5:5:2 wt. ratio) were mixed thoroughly. BZCYYb electrolyte powder with 1 wt.% ZnO sintering aid was blended with the ink vehicle (powder :vehicle = 4:5 wt.), then ground in a mortar until homogeneous electrolyte slurry was formed. 0.7 g cathode powders were pressed to pellets at 200 MPa in the 16 mm die, then spin-coated with two layers of BZCYYb electrolyte slurry. To increase the packing density of BZCYYb powders in the electrolyte layer, after drying at 120°C,

the anode/electrolyte bilayers were placed back to the die and pressed to 300 MPa for 1.5 min.[26] These pellets were sintered at 1300ºC for 4h in air. PBN-BZCYYb composite anode (0.5 cm^2 in area) was screen-printed to the electrolyte via the same route as in the half-cell. Pt paste was applied to the anode and cathode as the current collector. Silver wire was used as lead wire.

2.3 Characterization

Electrochemical measurements including symmetrical cell electrochemical impedance spectroscopy (EIS), full cell I-V curve, full cell EIS were carried out using Metrohm Autolab b.v. Impedance was collected over the frequency range from 1 MHz to 0.1 Hz with an AC perturbation of 10 mV. Different atmospheres were created via mass flow controllers (Alicat Scientific) and a temperature-controlled 30 L water bubbler with relevant carry gas. The resulting impedance spectra were analyzed by distributed relaxation time method (DRT)[29-31] and deconvoluted using Z-view 3.5 software. The microstructure of samples was examined by scanning electron microscopy (SEM, Hitachi S-4700).

3. Results

3.1 Lattice structure and chemical stability

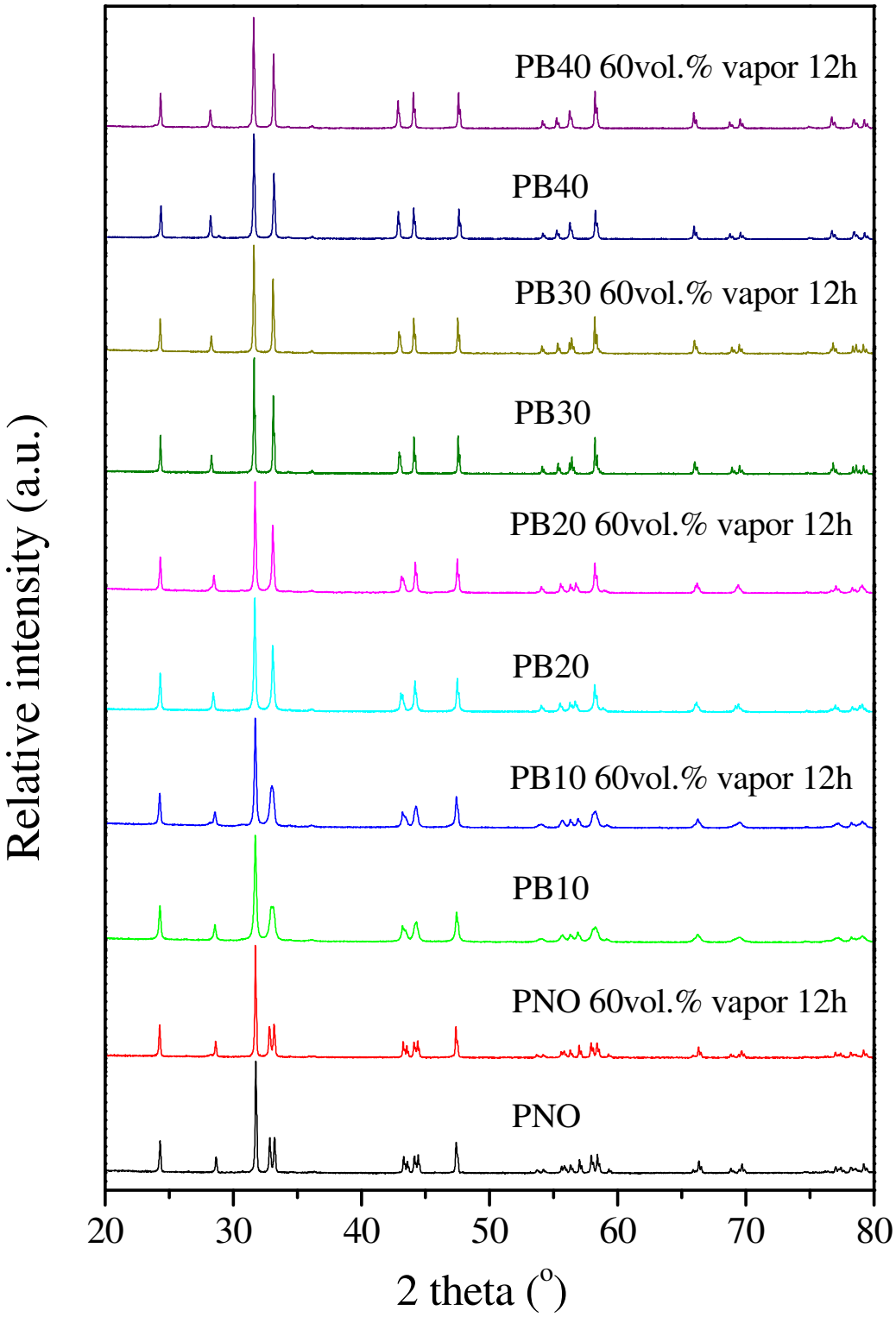

Fig. 1. XRD of as-prepared PBN samples and samples after treatment in steam.

Fig. 1 a shows the XRD pattern of PNO and Ba-doped PBN samples. PNO was verified as a pure phase with the orthorhombic structure. After substitution of larger size Ba (r_{Ba2+}=1.47Å) for Pr (r_{Pr3+}=1.179Å), PB10, 20, 30 and 40 all transferred to tetragonal structure. Fig. 1 b shows the stability of these samples treated in 60 vol.% water vapor mixed in air at 700ºC for 12h. The phase structure remained the same as in Fig. 1a and no foreign peaks were observed, verifying the chemical stability of PBN samples towards steam. Chemical compatibility with BZCYYb electrolyte was also confirmed on the powder samples after co-sintered at 1150ºC for 3h (Fig S1, XRD of treated PBN/BZCYYb mixture).

3.2 Triple-conducting electrode performance

Fig. 2a exhibits the Nyquist EIS plots for PBN samples measured at 600ºC in air with 60 vol.% water vapor. The electrode microstructure was shown in Fig. S2. The ohmic resistance was subtracted from these symmetrical cells. The area-specific resistance (ASR) was 0.207, 0.161, 0.143, 0.087 and 0.137 Ωcm^2 for PNO, PB10 to PB40, respectively. It decreased as increasing Ba content until PB30. Ba substitution promoted the water-splitting activity more than 100% on this PB30 sample compared to the pristine PNO. With more Ba added, the ASR started to increase for the PB40 sample. Fig. 2b summarizes ASRs of these samples measured in the intermediate temperature range of 550-700ºC in air with 60 vol.% water vapor. The same trend was held in every investigated temperature. Fig. 2c shows the overall activation energy E_a of these materials. All samples exhibited a similar E_a of ~1 eV for the water-splitting reaction. These impedance arcs were deconvoluted by software Z-view 3.5 to reveal the constituent components (see section 4.2 below for details on equivalent circuit construction and arc assignment based on DRT). The equivalent circuit (R_1//CPE1)-(R_2//CPE_2)-(R_3//CPE_3)-(R_4//CPE_4) and E_a of each elementary processes were presented in Fig. 3 (Fig. S3, Nyquist plot and fitting of PBN impedance). The resistance of the third arc from high to low characteristic frequency

order, R_3, was found the major contributor in all PBN samples except at 700ºC where this arc decreased to a similar magnitude of others. For comparison to other steam electrodes, table 1 summarizes the compositions and performance of popular steam electrodes for PCECs reported in recent years in the literature. Among all, PB30 samples delivered one of the best water-splitting performances.

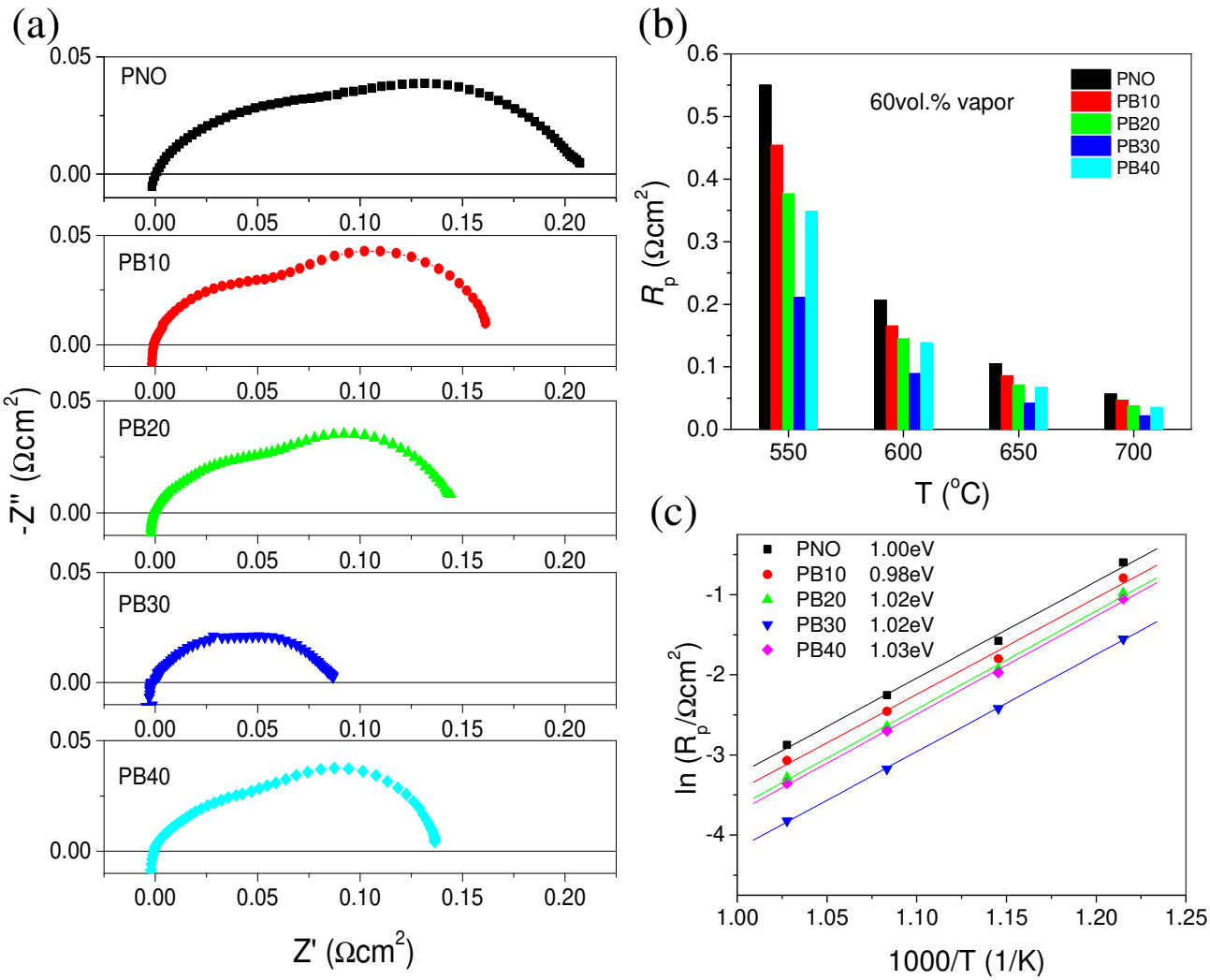

Fig. 2 (a) Nyquist plot of PBN samples measured in air with 60 vol.% water vapor at 600ºC, (b) comparison of polarization resistance of PBN at different temperature and (c) the corresponding apparent activation energy for ASR

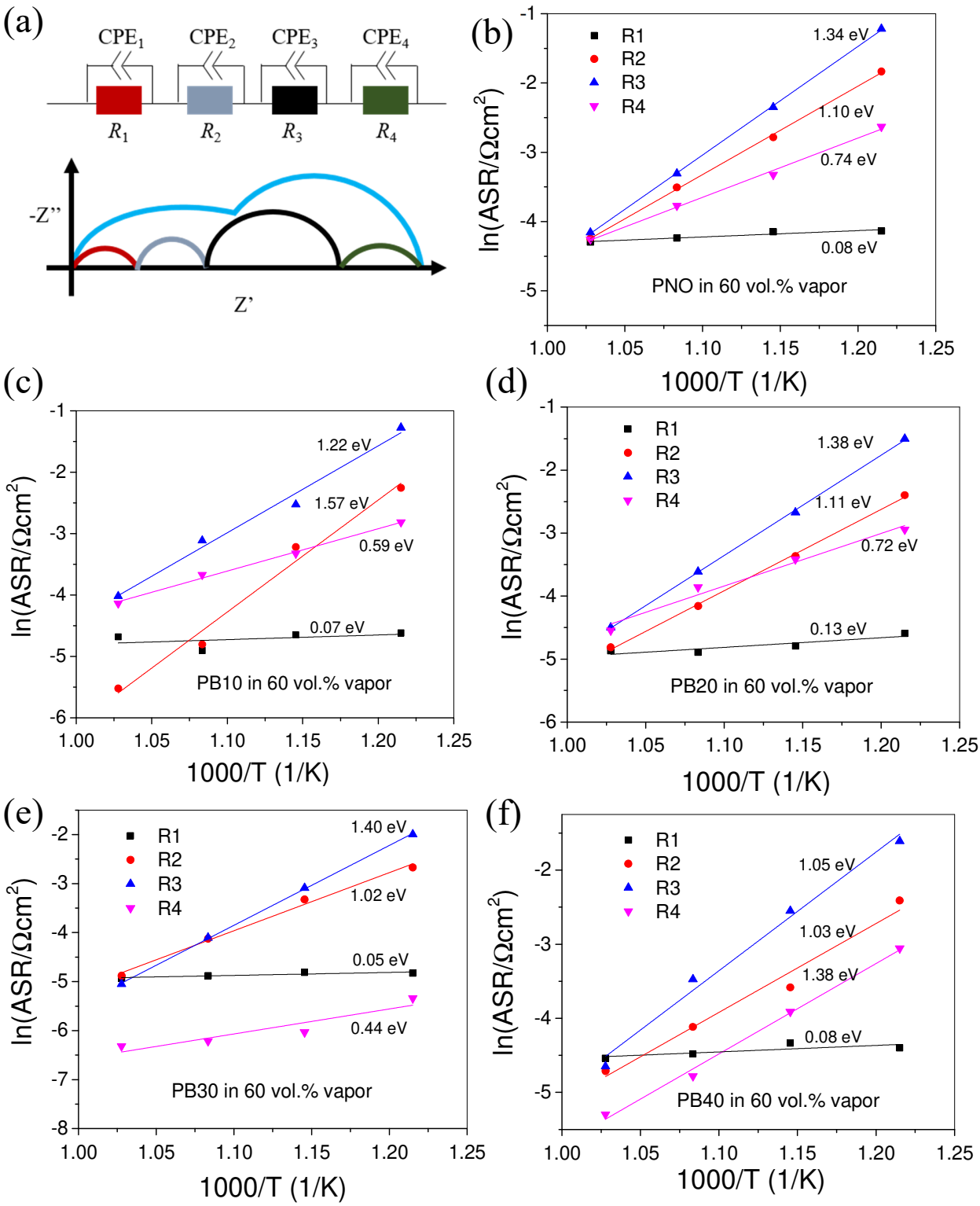

Fig. 3 (a) Equivalent circuit used to fit EIS, and a four-arc profile schematic, (b) to (f), the fitted resistance and E_a of these four arcs for electrode PNO, PB10 to PB40, respectively.

Table 1 Performance of recently reported high popular steam electrode candidates

Anode (composite)/electrolyte	Steam in anode (atm)	T (°C)	R_p (Ωcm^2) under OCV	Year and Ref
$Pr_{1.7}Ba_{0.3}NiO_{4+\delta}$/ $BaZr_{0.1}Ce_{0.7}Y_{0.1}Yb_{0.1}O_{3-\delta}$	0.6	700	0.022	This study
	0.6	600	0.089	This study
$La_{0.6}Sr_{0.4}Co_{0.2}Fe_{0.8}O_{3-\delta}$/$BaCe_{0.5}Zr_{0.3}Y_{0.16}Zn_{0.04}O_{3-\delta}$	0.03	800	0.36	2013[32]
$Ba_{0.5}Sr_{0.5}Co_{0.8}Fe_{0.2}$ $O_{3-\delta}$/$BaCe_{0.5}Zr_{0.3}Y_{0.16}Zn_{0.04}O_{3-\delta}$	0.03	800	0.075	2013[32]
$Sr_2Fe_{1.5}Mo_{0.5}O_{6-\delta}$ /$BaZr_{0.8}Y_{0.2}O_{3-\delta}$	0.03	600	0.48	2017[12]
$La_{0.6}Sr_{0.4}Co_{0.2}Fe_{0.8}O_{3-\delta}$/$BaCe_{0.2}Zr_{0.7}Y_{0.1}O_{3-\delta}$	2.5	700	0.7	2017[33]
$La_{0.8}Sr_{0.2}MnO_{3-\delta}$/$BaCe_{0.2}Zr_{0.7}Y_{0.1}O_{3-\delta}$	2.5	700	18	2017[33]
$Ba_{0.5}Sr_{0.5}Co_{0.8}Fe_{0.2}O_{3-\delta}$/$BaCe_{0.2}Zr_{0.7}Y_{0.1}O_{3-\delta}$	2.5	700	35	2017[33]
$La_{1.2}Sr_{0.8}NiO_{4+\delta}$/$BaCe_{0.7}Zr_{0.1}Y_{0.2}O_{3-\delta}$	0.2	700	0.27	2018[34]
$SrEu_2Fe_{1.8}Co_{0.2}O_{7-\delta}$/$Ba(Zr_{0.1}Ce_{0.7}Y_{0.2})O_{3-\delta}$	0.03	700	1	2018[35]
$SrEu_2Fe_{1.8}Co_{0.2}O_{7-\delta}$/$Ba(Zr_{0.1}Ce_{0.7}Y_{0.2})O_{3-\delta}$	0.03	600	6.8	2018[35]
$Nd_{1.95}Ba_{0.05}NiO_{4+\delta}$/$BaCe_{0.5}Zr_{0.3}Dy_{0.2}O_{3-\delta}$	0.03	750	2.3	2018[36]
$Nd_{1.9}Ba_{0.1}NiO_{4+\delta}F_{0.05}$/$BaCe_{0.5}Zr_{0.3}Y_{0.1}Yb_{0.1}O_{3-\delta}$	0.03	750	0.45	2020[37]
$PrNi_{0.5}Co_{0.5}O_{3-\delta}$ /$BaCe_{0.4}Zr_{0.4}Y_{0.1}Yb_{0.1}O_{3-\delta}$	0.1	450	0.32	2020[15]

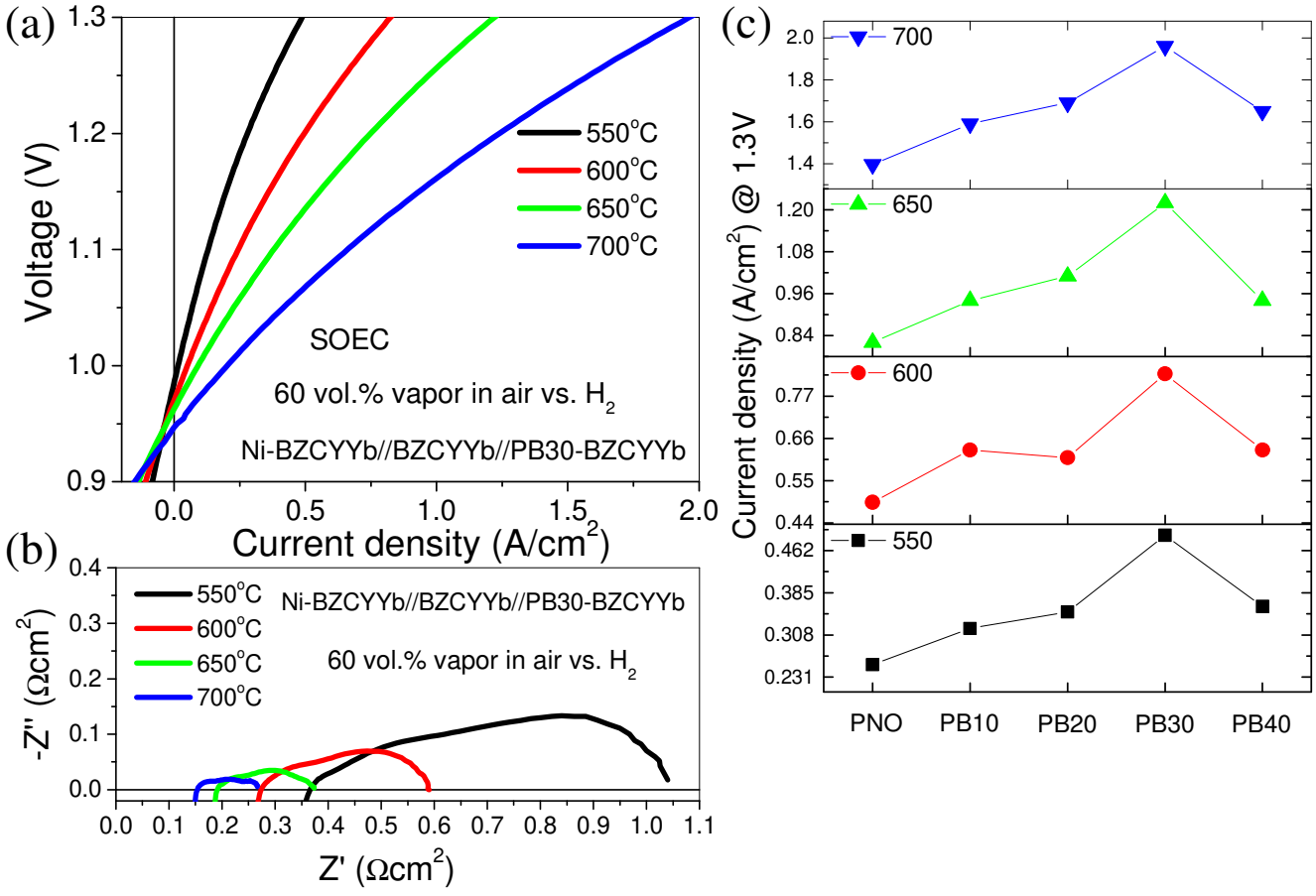

Fig. 4 (a) I-V curves of a cathode-supported cell with PB30 anode, (b) EIS of the corresponding full cell, (c) electrolyzing current densities of cathode-supported cells with different PBN steam electrodes measured from 550 to 700ºC at 1.3V applied potential.

Fig. 4a shows the performance of the full electrolysis cell with PB30 anode. A NiO-BZCYYb cathode-supported structure was adopted (Fig. S4, the microstructure of PBN full cells). During measurement, dry H_2 was fed to the Ni/BZCYYb cathode and 60 vol.% water vapor-containing air to the PB30/BZCYYb anode. The OCV was 0.980, 0.968, 0.963 and 0.946 V for temperatures from 550 to 700ºC, respectively. These values correspond to 96~97% of the theoretical Nernst potential,[38] verifying the gas-tightness of the thin-film electrolyte. The current density is 0.49, 0.83, 1.22 and 1.96 A/cm^2 from 550 to 700ºC at 1.3V, respectively. Fig. 4b is the corresponding EIS of the electrolysis cell. The polarization resistance was thermally activated from 0.67 Ωcm^2 at 550ºC to 0.11 Ωcm^2 at 700ºC. Ohmic resistance accounted for 35% of the overall ASR at 550ºC, but increased to 58% at 700ºC. At higher temperatures, the electrode polarization resistance was no longer the predominant limiting factor of the performance. By referring to the steam electrode performance in Fig. 2a, it is revealed that this PB30 steam electrode only accounted for 31%, 28%, 23%, and 19% of the electrode resistance from 550 to 700ºC. The major portion of the polarization resistance was from the Ni-BZCYYb cathode in this PB30 cell. These results have proven the effectiveness of this RP phase triple-conducting material in promoting the water-splitting reaction kinetics.

Table 2 Comparison of electrolysis performance of PCECs with popular steam electrodes at 600ºC.

Cell configuration	Steam in anode (atm)	Polarization resistance (Ωcm^2)	Current density (A/cm^2)	Overpotential at 1.3 V applied potential (V)	Year of Ref
$Pr_{1.7}Ba_{0.3}NiO_{4+\delta}$-BZCYYb//$BaZr_{0.1}Ce_{0.7}Y_{0.1}Yb_{0.1}O_{3-\delta}$(15)//Ni-BZCYYb	0.6	0.34	0.83	0.33	This work
$Sm_{0.5}Sr_{0.5}CoO_{3-\delta}$-BCZY//$BaCe_{0.5}Zr_{0.3}Y_{0.2}O_{3-\delta}$(20 μm)//Ni-BCZY	0.5	2.5	0.15	0.35	2010
(LaSr)$CoO_{3-\delta}$-BCZYbCo//$BaCe_{0.48}Zr_{0.4}Yb_{0.1}Co_{0.02}O_{3-\delta}$ (45 μm)//Ni-BCZYbCo	0.3	-	0.03	0.32	2011[39]
$La_{0.6}Sr_{0.4}Co_{0.2}Fe_{0.8}O_{3-\delta}$-BZY20//$BaZr_{0.8}Y_{0.2}O_{3-\delta}$ (15 μm)//Ni-BZY20	0.03	-	0.053	0.45	2015[5]
$LaNi_{0.6}Fe_{0.4}O_{3-\delta}$/$La_2NiO_{4+\delta}$-BCZD//$BaCe_{0.5}Zr_{0.3}Dy_{0.2}O_{3-\delta}$ (30 μm)//Ni-BCZD	0.9	-	0.17	0.34	2016[40]
$Sr_2Fe_{1.5}Mo_{0.5}O_{6-\delta}$-BZY//$BaZr_{0.8}Y_{0.2}O_{3-\delta}$ (16 μm)//Ni-BZY	0.03	-	0.21	0.44	2017[12]
$(La_{0.8}Sr_{0.2})_{0.98}MnO_3$-BCZI//$BaCe_{0.5}Zr_{0.2}In_{0.3}O_{3-\delta}$ (15 μm)//Ni-BCZI	0.2	4.2	0.10	0.3	2017[41]

$Pr_2NiO_{4+\delta}$-BZCY//$BaZr_{0.2}Ce_{0.6}Y_{0.2}O_{3-\delta}$ (20 μm)//Ni-BZCY	0.4	0.4	0.36	0.33	2018[11]
$Ba_{0.5}La_{0.5}CoO_{3-\delta}$//$SrZr_{0.5}Ce_{0.4}Y_{0.1}O_{2.95}$ (17 μm)//Ni-SZCY541	0.8	-	0.25	0.7	2018[42]
$Pr_{1.2}Sr_{0.8}NiO_4$//$BaCe_{0.7}Zr_{0.1}Y_{0.2}O_{3-\delta}$ (15 μm)//Ni-BCZY	0.2	2.17	0.35	0.3	2018[34]
$La_{1.2}Sr_{0.8}NiO_4$//$BaCe_{0.7}Zr_{0.1}Y_{0.2}O_{3-\delta}$ (15 μm)//Ni-BCZY	0.2	1.47	0.42	0.3	2018[34]
$Nd_{1.95}Ba_{0.05}NiO_{4+\delta}$-BCZD//$BaCe_{0.5}Zr_{0.3}Dy_{0.2}O_{3-\delta}$ (15 μm)//Ni-BCZD	0.3	0.44	0.16	0.33	2018[36]
$SrEu_2Fe_2O_{7-\delta}$-BZCY//$Ba(Zr_{0.1}Ce_{0.7}Y_{0.2})O_{3-\delta}$ (15 μm)//Ni-BZCY	0.1		0.21	0.23	2018[35]
$Sr_{2.8}La_{0.2}Fe_2O_{7-\delta}$//$BaZr_{0.3}Ce_{0.5}Y_{0.2}O_{3-\delta}$ (20 μm)//Ni-BZCY	0.2	2.0	0.46	0.34	2018[13]
$SrEu_2Fe_{1.8}Co_{0.2}O_{7-\delta}$-BZCY//$Ba(Zr_{0.1}Ce_{0.7}Y_{0.2})O_{3-\delta}$ (15 μm)//Ni-BZCY	0.1	0.9	0.40	0.33	2018[35]
3D-$PrBa_{0.5}Sr_{0.5}Co_{2-x}Fe_xO_{5+\delta}$//$BaZr_{0.1}Ce_{0.7}Y_{0.2-x}Yb_xO_{3-\delta}$ (10 μm)//Ni-BZCYYb	0.12	-	0.75	0.31	2018[17]
$PrBa_{0.5}Sr_{0.5}Co_{2-x}Fe_xO_{5+\delta}$//$BaZr_{0.1}Ce_{0.7}Y_{0.2-x}Yb_xO_{3-\delta}$ (10 μm)//Ni-BZCYYb	0.12	-	0.48	0.31	2018[17]
$PrBa_{0.5}Sr_{0.5}Co_{1.5}Fe_{0.5}O_{5+\delta}$ PLD-modified//$BaZr_{0.4}Ce_{0.4}Y_{0.1}Yb_{0.1}O_3$ (15 μm)//Ni-BZCYYb	0.03	0.34	1.92	0.27	2019[18]
$BaCo_{0.4}Fe_{0.4}Zr_{0.1}Y_{0.1}O_{3-\delta}$//$BaCe_{0.7}Zr_{0.1}Y_{0.1}Yb_{0.1}O_{3-\delta}$ (15 μm)//Ni-BZCYYb	0.1	-	1.1	--	2019[22]
$BaGd_{0.8}La_{0.2}Co_2O_{6-\delta}$-BZCY//$BaZr_{0.7}Ce_{0.2}Y_{0.1}O_{2.9}$//Ni-BZCY	1.5	1.1	0.1	0.35	2019[43]
$Nd_{1.9}Ba_{0.1}NiO_{4+\delta}F_{0.05}$//$BaCe_{0.5}Zr_{0.3}Y_{0.1}Yb_{0.1}O_{3-\delta}$ (25 μm)//Ni-BCZYYb	0.5	2.5	0.36	0.31	2020[37]
$PrNi_{0.5}Co_{0.5}O_{3-\delta}$ //$BaCe_{0.4}Zr_{0.4}Y_{0.1}Yb_{0.1}O_{3-\delta}$ (15 μm)//Ni-BCZYYb	0.1	-	0.83	0.26	2020[15]

Fig. 4c summarizes the performance of all cathode-supported full electrolysis cells with those PBN anodes (Fig. S5, IV curves for electrolysis cells with PBN anodes). These cells were measured under the same condition as the PB30 sample. The performance of these electrolysis cells at low temperatures was more different from each other compared to the high-temperature end. At higher temperatures, the difference became marginal, most likely because the performance was then determined more by the Ni-BZCYYb cathode and the electrolyte ohmic resistance. Compared to the most recent various PCECs as summarized in Table 2, the present PCEC with PB30 anode showed one of the best performances. Few other reports in the literature achieved higher performance at this intermediate temperature range.[18, 22, 44] In some of those studies, sophisticated electrode microstructure engineering, such as 3D pattern electrode[44] or pulsed laser deposition layer modification,[18] had been explored to boost the output performances.

4. Discussion

4.1 Proton conduction in RP phase PBN samples

Ba substitution significantly improved the performance of this triple-conducting RP phase anode. Although this "triple-conducting" term was coined years ago[20] and a great number of related materials have been investigated by co-workers later on, the importance of each conductivity in the performance and how they possibly affect the reaction rate have not been investigated to the best of

our knowledge. As a case study, these PBN samples are further analyzed to shed light on the underlying mechanism of the high performance achieved by the triple-conducting materials.

One probable decisive factor of the electrode performance could be the proton conductivity. In the material design, this property is the central role to expand the reactive network from 3PB lines to 2PB inner surfaces. It removes the site limitation on the proton incorporation, facilitates a continuous bulk proton-conducting network in the anode bulk. However, a direct electrical measurement of the proton conductivity is difficult at this moment. Electrode candidates for solid oxide cells usually possess dominant electronic conductivity as well as oxygen conductivity on top of proton conductivity. And PNO is chemically incompatible with reducing atmosphere. An appropriate blocking electrode is needed but still not available, since most of them possess oxygen conductivity as well. Few reports regarding the proton conductivity of these PCEC electrode materials were published in the literature.[45] In the present study, we tried a new route. We probe the proton conduction property by monitoring the transition of the electrical conductivity that can be affected by the introduction of protons to the lattice. PBN bar samples with identical dimensions 10×3×3 mm were fabricated. During measurement, a certain PBN sample was isothermally held at 600ºC in a ~0.9 L tube furnace. The sample was first equilibrated in pure N_2 for a stable electrical conductivity. The atmosphere was then switched from N_2 to 60 vol.% water vapor containing N_2 at a flow rate of 500 sccm. The transition of the electrical conductivity to a new equilibrium was recorded. Fig. 5 shows the transition processes of all PBN samples. Oxygen in the ultra-high purity N_2 used here was ~1 ppm. Oxygen in the 60 vol.% water vapor containing N_2 was from both N_2 carry gas and the pyrolysis of steam. It can be calculated as 0.86 ppm. Therefore, there was only a trace amount of oxygen in the sample chamber and its change between the two stages was marginal. The effect of $p(O_2)$ is neglected here.

After the introduction of steam, the conductivity decreased in all samples, in a range of 0.8~1.3 S/cm. This change is too big to come from the oxygen or proton conductivity. It must be majorly from the electronic conductivity. Two possible interactions between the PBN sample and steam can be described below in Kröger-Vink notation:

Net H_2O intake $$H_2O + O_O^x + V_i^x \leftrightarrow HO_O^\bullet + HO_i' \quad (1)$$

H_2O intake with the release of O_2 $$H_2O + 2O_O^x + 2h \leftrightarrow 2HO_O^\bullet + 0.5O_2 \quad (2)$$

The first interaction shows net water intake without involving any electronic charge carrier, therefore will not affect the electronic conductivity. The second interaction, on the other hand, shows that for every H_2O molecule intake, two electronic holes will be consumed. RR phase nickelates are known as p-type conductors.[27, 46] Loss of charge carrier will lower the electronic conductivity, which is consistent with the observed phenomena. (Note: the evidence supporting the second interaction does not exclude the co-existence of the first one. As the first interaction does not affect the electronic conductivity, its presence cannot be determined through this testing.) As the water intake proceeds, a new, stable electronic conductivity will not be reached until protons spread from the surface to the core of the sample through proton-electron bipolar diffusion, and until finally distributed over the entire bulk of the sample evenly. This transition process is thus a good descriptor of the proton conductivity of these PBN samples considering the electron conduction is much faster than the proton. The transition time is extracted between two equilibrium stages and marked on each plot in Fig 5. Substitution of Ba monotonically decreased this time from 2318 s for PNO to 294 s for PB40, or in other words, increased the proton conductivity. However, this finding is not in complete agreement with the polarization resistance testing, in which the performance of PBN samples peaked at PB30 and went down for the PB40 sample. It means that proton conductivity alone cannot account for the performance change of these PBN materials.

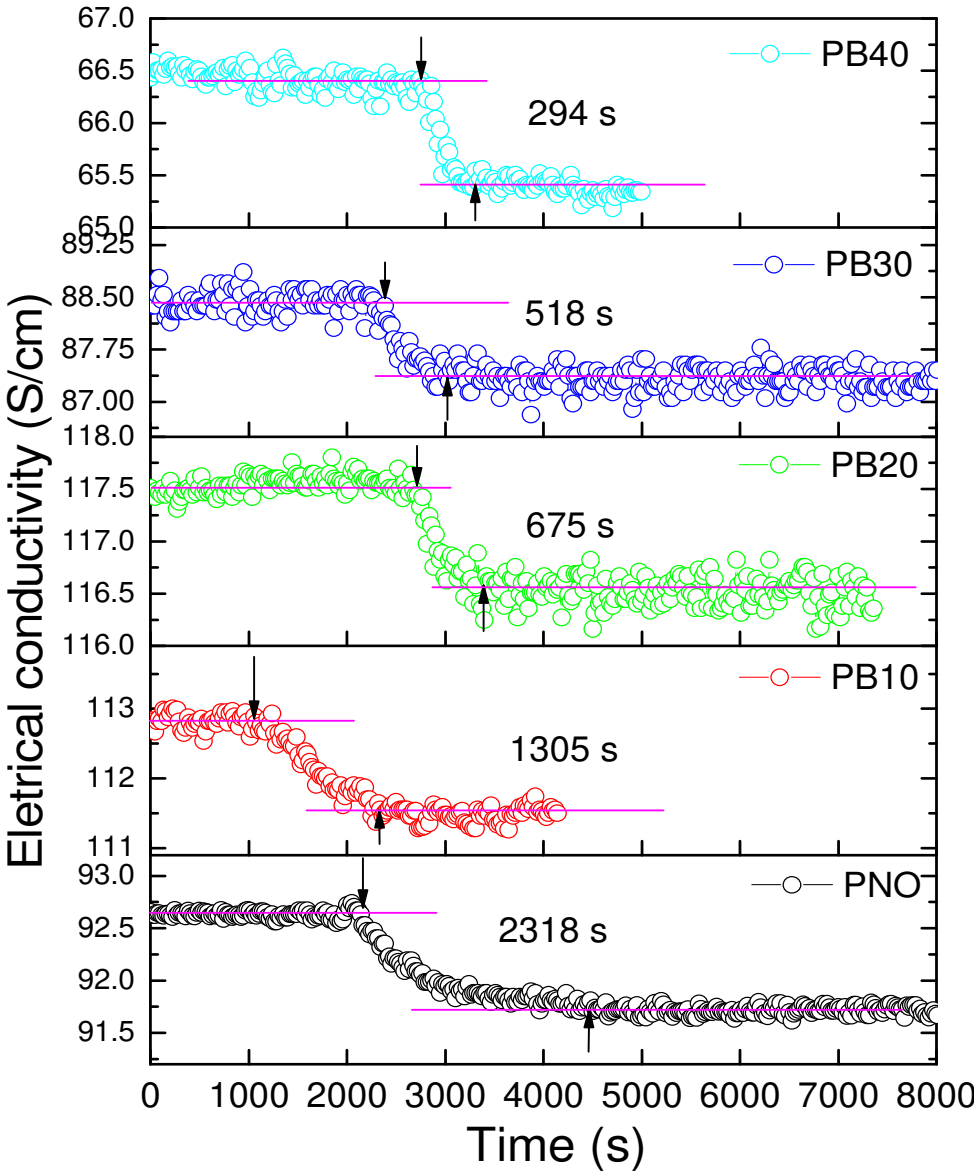

Fig. 5 Transition of the electrical conductivity of PBN samples upon gas atmosphere shift from dry N_2 to 60 vol.% water vapor containing N_2.

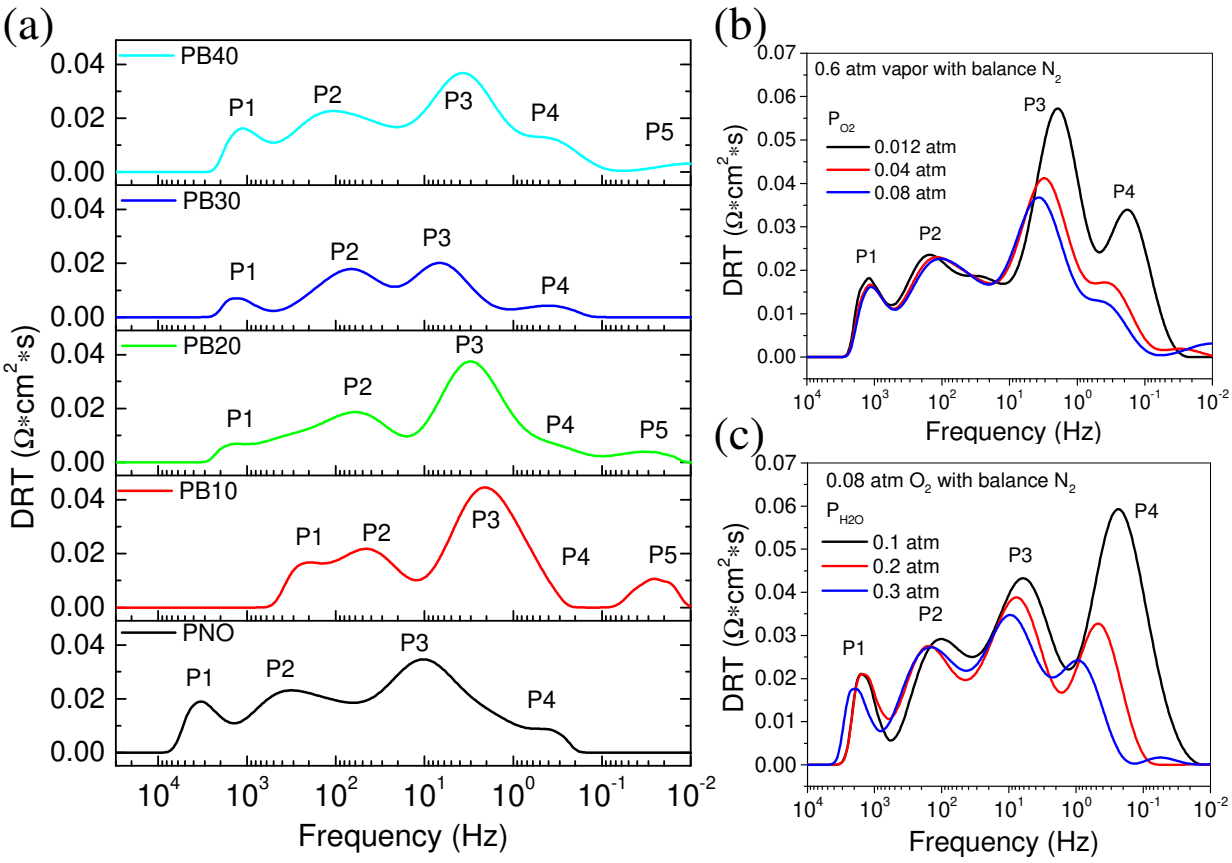

Fig. 6 (a) DRT deconvolution of polarization resistance of PBN samples measured in 60 vol.% water vapor containing air at 600ºC, (b) dependence of PB40 sample toward oxygen content, (c) dependence of PB40 sample towards water vapor content.

4.2 Rate-limiting oxygen-related surface processes

To gather in-depth insight into the polarization resistance, DRT was used to de-convolute the impedance spectroscopy of these PBN samples. Fig. 6a shows the DRT analysis of spectra measured at 600ºC in 60 vol.% water vapor-containing air. The peaks are marked in order from high to low frequency. Four peaks can be found for all samples (P5 is minor and not present for all samples, thus left out here). Therefore, four (R//CPE) units in the series were used as the equivalent circuit to represent the reaction process. The area of the peak corresponds to the resistance of the related process. Of these four peaks, P3 is the dominant one, as evidenced in Fig. 3b-f. It largely determines the overall

polarization resistance and shows the same trend as the ASR in Fig. 2b. As Ba content increased, the area of this peak decreased until PB40. P3 for PB40 otherwise enlarged from that of PB30. Therefore, this peak, as a major contribution to the ASR, cannot be assigned to the proton conducting resistance, which is consistent with the previous judgment that proton-conducting is not the sole factor determining the polarization resistance.

To find out the nature of these peaks, their dependence on the reactants was evaluated. PB40 was measured with varying $p(H_2O)$ or $p(O_2)$. Variation of gas content in the sample chamber was realized by adjusting the amount of steam, O_2, and N_2 altogether. Steam and O_2 were the active gas to be changed, and N_2 worked as the balance gas to compensate for the change. Fig. 6b shows the DRT results of PB40 measured at 600ºC under fixed 60 vol.% steam. O_2 content was varied from 0.012 to 0.08 atm. P1 and P2 were irresponsive to $p(O_2)$. Both P3 and P4 showed apparent dependence on $p(O_2)$. Fig. 6c exhibits the response of PB40 to the change of $p(H_2O)$ at 600ºC under fixed 8% O_2. Steam content was varied from 0.1 to 0.3 atm. Likewise, P1 and P2 were not sensitive to $p(H_2O)$. But P3 and P4 both showed a response to $p(H_2O)$, except for the latter being more evident.

For this protonic ceramic electrolysis system, a micro-kinetics model of water-splitting can be constructed to tackle this involved process. A possible case is represented as follows:

Step 1: H_2O adsorption	$H_2O \leftrightarrow H_2O_{ads}$	$p(H_2O)$	(3)
Step 2: H_2O dissociation	$H_2O_{ads} + O^{x}_{O,PBN} + V^{x}_{i} \leftrightarrow HO^{\bullet}_{O,PBN} + HO'_{i,PBN}$	$p(H_2O)$	(4)
Step 3: Proton carrier shift	$HO'_{i,PBN} + O^{x}_{O,PBN} \leftrightarrow O''_{i,PBN} + HO^{\bullet}_{O,PBN}$	$p(H_2O)$	(5)
Step 4: Proton diffusion	$HO^{\bullet}_{O,PBN}$_hgh conctr loc↔ $HO^{\bullet}_{O,PBN}$_lw conctr loc	Constant	(6)
Step 5: Proton transfer	$HO^{\bullet}_{O,PBN} + O^{\times}_{O,BZCYYb} \leftrightarrow O^{x}_{O,PBN} + HO^{\bullet}_{O,BZCYYb}$	Constant	(7)
Step 6: Oxygen diffusion	$O''_{i,PBN}$_hgh conctr loc↔ $O''_{i,PBN}$_lw conctr loc	Constant	(8)
Step 7: First charge transfer	$O''_{i,PBN} \leftrightarrow O'_{ads} + V^{x}_{i} + e$	$p^{\frac{3}{4}}(H_2O)p^{\frac{1}{8}}(O_2)$	(9)
Step 8: Second charge transfer	$O'_{ads} \leftrightarrow O_{ads} + e$	$p^{\frac{1}{4}}(H_2O)p^{\frac{3}{8}}(O_2)$	(10)

Step 9: Oxygen association	$2O_{ads} \leftrightarrow O_{2,ads}$	$p(O_2)$	(11)
Step 10: Oxygen desorption	$O_{2,ads} \leftrightarrow O_2$	$p(O_2)$	(12)

This micro-kinetics model is not meant to be exclusive. Other models with elemental processes using different defects in different ways are also possible. RP phase possesses two kinds of active defects, namely, interstitial site-interstitial oxygen pair and lattice oxygen-lattice oxygen vacancy pair. The present elemental steps are chosen in consideration of certain general rules and RP material-specific facts: (a) a truly elementary charge transfer step only involves the exchange of one electron (that is, $O''_{i,PBN} \leftrightarrow O_{ads} + V_i^x + 2e$ is not a realistic elementary step.[47] (b) O_{ads}^{2-} is not stable on the electrode surface, therefore the first charge-transfer proceeds with the interstitial oxygen underneath the surface,[48] (c) two diffusion steps, step 4 and 6, are presented to reflect the oxygen and proton-conducting capability of this triple-conducting anode; (d) $V_o^{\bullet\bullet}$is not presented here because of its low population inside the RP phase. The formation of $V_o^{\bullet\bullet}$ is governed by the Frenkel disorder, $O_O^{\times} = O_i'' + V_O^{\bullet\bullet}$. As reported by Nakamura et al,[49] ΔG^0 is 246 kJ/mol for this reaction at 700°C in RP phase $La_2NiO_{4+\delta}$, which means at oxygen hyperstoichiometric region $[V_O^{\bullet\bullet}]$ is at most 2.5×10^{-7} per unit cell.

The dependence of these steps on $p(H_2O)$ and $p(O_2)$ expressed in reaction order was calculated and listed after each equation. Among them, only step 7 and 8 show dual-dependence. This dual-dependence is coincident with the behavior of P3 and P4 in Fig. 6b and c. Judging by the dependence weight, P3 is more likely to correspond to step 8, and P4 to step 7. These are two charge transfer steps that can be activated readily by the applied potential. However, if this assignment is right, one will easily find that the performance of these PBN samples has little to do with the proton conductivity, but is heavily determined by the oxygen-related surface processes. To verify this judgment, the oxygen

exchange activity of these PBN was assessed by the electrical conductivity relaxation (ECR) method.[50-52]

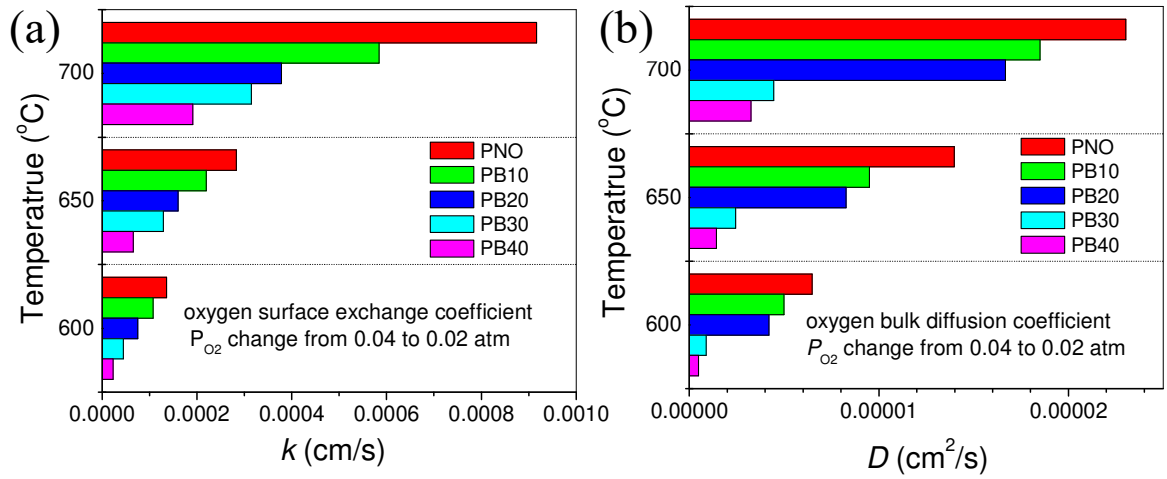

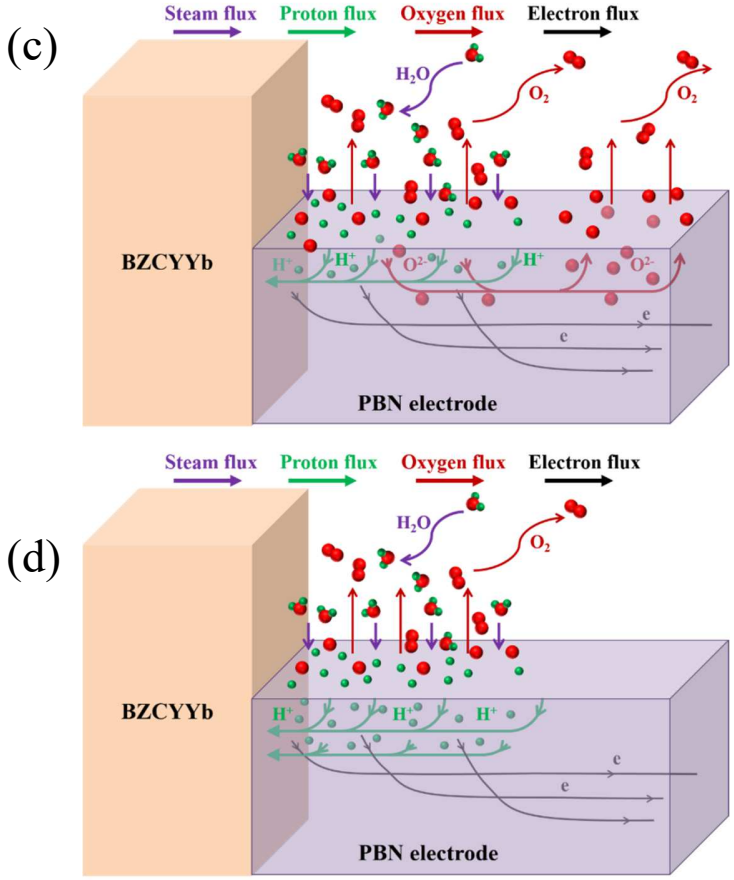

Fig. 7 (a) oxygen surface exchange coefficient (*k*) and (b) bulk diffusion coefficient (*D*) of PBN samples measured under $p(O_2)$ change from 0.04 to 0.02 atm at different temperatures, (c) a scenario of reaction pathway for a triple-conducting steam electrode, (d) the real reaction pathway of the PBN steam electrode, oxygen conduction is not pertinent.

To avoid any interference from water vapor but only focus on oxygen, dry oxygen-containing gases were used all the time. A dense PBN bar sample was soaked in 0.04 atm O_2 balanced by N_2 and heat to 600ºC. When the electrical conductivity was stabilized, the gas atmosphere was switched from 0.04 to 0.02 atm O_2. The electrical conductivity relaxation process was monitored. The standard ECR procedure can be found elsewhere in detail.[53, 54] During this process, the chemical interaction between the PBN sample surface and the surrounding atmosphere can be expressed as:

$$O_2 + 2V_i^x \leftrightarrow 2O_{i,PBN}'' + 4h \quad (13)$$

The surface oxygen exchange coefficient (*k*) characterizes the kinetics of this reaction. This equation is an overall expression that consists of step 7 to 10 with step 7 and 8 being the rate-limiting ones. Therefore, *k* value will be diminished if the kinetics of step 7 and 8 are sluggish. Another involved process during the re-equilibration is the diffusion of $O_{i,PBN}''$ defects inside PBN bar samples, which corresponds to the bulk diffusion coefficient (*D*). *k* & *D* results for PBN samples are exhibited in Fig. 7 (Fig. S6, ECR fittings of PBN samples with *k* & *D* values). It is found that *k* value decreases monotonically from PNO to PB40. This result is not surprising from the viewpoint of how RP phase works to exchange oxygen. For RP phase materials, interstitial oxygen, $O_{i,PBN}''$, was previously proven to play a determining role of the surface exchange activity. Interstitial oxygen in form of δ in this $Pr_{2-x}Ba_xNiO_{4+\delta}$ formula was determined through our iodine titration as 0.256, 0.132, 0.097, 0.058, 0.010 for PNO to PB40. *k* value decreases drastically with the decreasing inventory of active $O_{i,PBN}''$. This monotonic trend of *k* however predicts that if step 7 and 8 are the rate-limiting processes in the steam

electrodes, the polarization resistance should keep increasing from PNO to PB40, which is still not true.

To reconcile this paradox, we need to revisit the implication in the micro-kinetics model. Micro-kinetics models characterize the reaction kinetics in a localized, atomic level, without explicit involvement of the spatial distribution of the active sites. On the other hand, the measured data represent the comprehensive reaction activity, which will be affected not only by the intrinsic reaction rate of each step listed through step 1 to 10, but also by the availability of active sites inside the electrode bulk. This is especially true for materials with significant ionic conductivities that can expand the reaction site from 3PB lines to 2PB areas to a certain extent, depending on the magnitude of these conductivities. The inclusion of this spatial expansion of active sites whose cumulative area is different between different samples forbids direct comparison of polarization resistance between these samples. That is, even though a certain reaction X is intrinsically fast on sample 1 than on sample 2, but the measured resistance for reaction X could still be larger on sample 1 than on sample 2 if sample 2 provides more reaction sites for this reaction. This interplay between the intrinsic reaction rate (reaction rate normalized to active surface area) and the availability of active sites is most likely the underlying reason responsible for the volcano performance trends from PNO to PB40. The kinetics of step 7 and 8 being the rate-determining steps in the micro-kinetics model truly slows down from PNO to PB40. However, due to the increase of proton conductivity from PNO to PB40, the proton-conducting network expands to provide more available active surfaces for these reactions. The final result out of competition of these two reverse trends is that the performance peaks at PB30. Beyond this, the loss of the surface oxygen removal rate outweighs the active site gain from higher proton conductivity and leads to a performance downgrade.

On the other hand, the expansion of the reactive network would come at the expense of proton diffusion resistance. As the active area expands to more PBN surfaces, the average diffusion length for a proton to transport from the surface reaction site through the electrode bulk to the electrolyte increases, leading to a perceptible ionic resistance. The ion diffusion length in a practical porous MIEC electrode has been well-documented in oxygen-conducting solid oxide cells by Adler etc.[55, 56] It can be as large as 20 μm at 700°C. This characteristic length is determined by operating temperature, *D* & *k* values of the material, and the microstructure of the electrode. This diffusion is not a clean-cut, end-to-end process but coupled with surface reactions along the diffusion path that generates more ion species to join the flux. Therefore, instead of appearing as an ohmic resistance in the impedance, this process manifests itself in the high-frequency section of the arc. A transmission line equivalent circuit model is generally used to account for this involved process, from which the diffusion contribution to the high-frequency arc has been readily witnessed.[57-59] In the present case, it means that the proton diffusion resistance will be caught by the EIS in the polarization resistance part. According to the dependence of these peaks on reactants in the DRT analysis in Fig. 6b and c, P2 can be assigned to this proton diffusion process. This peak shows no dependence to $p(O_2)$, and weak dependence to $p(H_2O)$ given that the concentration of protons inside the PBN lattice could increase when $p(H_2O)$ changes from 0.1 to 0.3 atm. This behavior is still consistent with the "Constant" prediction in the micro-kinetic model where no change of catalytic material itself vs. reactant has been taken into account. A marked observation about P2 is that this peak does not show any trend with Ba content as indicated in Fig. 3, that is, the faster proton-conduction in Ba-richer samples does not necessarily result in a smaller proton diffusion resistance in the electrode. This phenomenon is not surprising. Sample, like PB40, with higher proton conductivity but slower surface oxygen removal rate, would show a larger characteristic length than PNO. The final proton diffusion resistance

depending on both the conductivity and the characteristic length. Thus, there may not be a simple trend following either factor.

Besides proton-conduction, oxygen-conduction is also a property of these PBN materials. But the aforementioned role of proton-conduction could not possibly be replaced by oxygen-conduction. ECR results in Fig. 7 show both oxygen surface exchange and bulk diffusion linearly decreased with Ba substitution. Therefore, a performance downgrade from PNO to PB40 would have resulted if the expanded reactive network was mainly established by the oxygen diffusion. To visualize this difference, a comparison of reaction pathways is illustrated in Fig. 7 c and d, showing a scenario case that utilizes each conducting ability of this triple-conducting electrode, and the real case that expands the active inner surface through proton-conduction. The so-called "triple-conducting" electrode would be valid both in name and in fact if the reaction pathway is indeed as shown in Fig 7c. However, in reality, the proton-conducting rail eclipses the oxygen-conducting rail, making the oxygen-conductive an empty claim in the triple-conducting property. And the water-splitting reaction proceeds as shown in Fig. 7d.

4.3 Influence of the electronic contribution

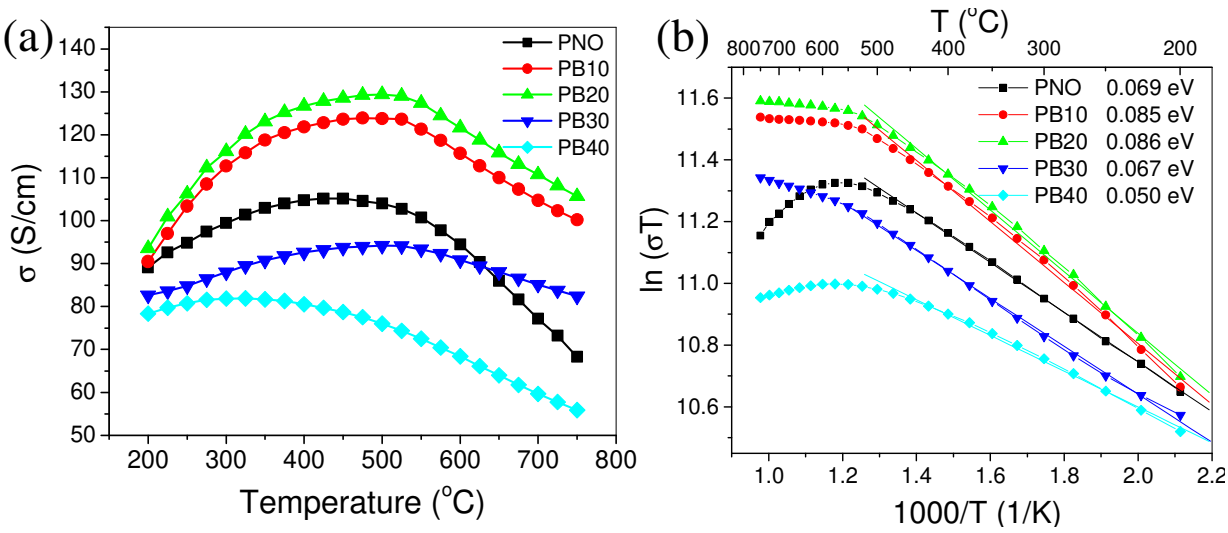

Fig. 8 (a) Four-probe DC electrical conductivity of PBN samples, (b) Arrhenius plot with activation energies

Fig. 8 displays the electrical conductivities and activation energies of these PBN samples. Within the operating temperature range from 550 to 700ºC, the minimum value is 57 S/cm from PB40 at 700ºC. Again, the electrical conductivities will typically be 2 to 3 orders of magnitude higher than the oxygen or proton conductivities in PBN samples. Thus, these values can be reasonably taken as electronic conductivity. Usually, the conductivity of a porous electrode is ~1/10 of the intrinsic value measured from dense bulk samples. The contribution of the conduction resistance of the electronic defects in the electrode resistance can be calculated as ~3.5×10^{-4} Ωcm^2 for a 20 μm thick electrode. This is a marginal value compared to the ASR. Nevertheless, the electronic conductivity may be a mediator of the charge transfer kinetics if the charge transfer is limited by the activity of the electrons instead of the ionic species. A significant increase of oxygen reduction kinetics has been observed on materials with improved electronic conductivity though their activity of oxygen defects largely remained similar.[60-63] However, in the present case, there lies no correlation between this conductivity and the polarization resistance. The electronic conductivity ranks in order PB20>PB10>PNO>PB30>PB40 at 550-700ºC range, totally different from the trends in the charge transfer processes of P3 and P4 in Fig. 6 or R3 and R4 in Fig. 3. In addition, these resistance peaks showed apparent dependence on the reactants, meaning that the ionic species is more important to the charger transfer steps.

There is one last process left to assign, P1. It is noteworthy that this high-frequency peak showed very weak thermal activation during testing in Fig. 3. The nature of the peak is not fully understood yet. Elementary steps 1-10 all have a strong thermal activation effect. Another reported common step that has weak thermal activation is the gas diffusion process.[64, 65] But the characteristic frequency

(1500-3400 Hz) of P1 is too high for gas diffusion.[66, 67] And the gas diffusion resistance is also highly impossible to be detected by EIS at open circuit conditions in a 20 μm thin electrode.[68] This peak is not responsive to any reactant changes as shown in Fig. 6c and d. In this regard, we tentatively assign this high-frequency process (0.008-0.014 Ωcm^2 for different PBNs) to the contact resistance between the Pt current collector and the PBN electrode. The interface metal/ceramic multi-point contacts would create a space charge layer, therefore introducing a capacitive behavior to the EIS arc. It is a resistance of conduction in nature, hence showing no dependency on the surrounding gases. The activation energy of this resistance could be complicatedly determined by the barrier height of the space charge layer, the temperature dependence of metallic Pt and ceramic PBN altogether. The magnitude of this resistance is roughly close to each other for all specimens but shows no direct correlation to the measured electrical conductivity of PBNs. It may be due to that the Pt/PBN interface barrier height is not solely indicative of the conductivity of PBNs, or simply due to the technical scattering in the manual fabrication of the current collector (Pt current collector was applied by hand, instead of screen-printing in consideration of material cost). Although very small, this resistance still appeared as a perceptible source of resistance when the operating temperature ramped up to 700°C, especially for the candidate with very small ASR like PB30 and PB40.

It comes clear that new triple-conducting steam electrode materials could behave much differently from their oxygen-conducting MIEC predecessors. Within the application in PCECs, the co-existence of proton and oxygen ionic species changes the oxygen dominancy in MIEC. The contribution of oxygen conduction can be trivial, as the highly conductive competitor species, e.g. proton here would damp its real effect on the surface/bulk intertwined reaction set in a practical porous structure, or in other cases, proton and oxygen vacancy are just a trade-off pair, and proton conduction takes the dominancy when steam is supplied.[69, 70] In the end, oxygen-related influence could be only limited

to the electrode surface. It then provides a new vision that in a PCEC steam electrode surface modification that predominantly tunes the activity towards oxygen removal could promote its catalytic performance to another level.

3. Conclusion

Based on RP phase PNO, a case study was carried out to illuminate the correlation of each conducting rail of the electron, proton, and oxygen-triple conductors to their performance as steam electrodes toward water-splitting reaction in PCECs. Pr-site Ba substitution gradually tuned each conductivity, providing an effective case to probe the underlying causes that are responsible for the superior electrode performance. Of those three conducting rail, electronic conductivity was found not a direct limiting factor. It neither added to the ohmic resistance nor limited the charge transfer steps. But a possible electron transfer resistance at the current collector/electrode junction could introduce a noticeable resistance to the ASR at high temperature. Proton conducting was predictably crucial to the performance. It was responsible for an expanded active network that provided more active sites for faster surface adsorption of water and desorption of oxygen. The effect of oxygen conducting was surprisingly not significant to the reaction kinetics. It cast no noticeable influence on the spatially distributed reaction pathway in the RP phase candidates. The much faster proton conduction seemed to eclipse the sluggish oxygen conduction to transport ionic special between the reactive surfaces and electrolyte. On the contrary, the surface oxygen exchange activity was found rate-limiting. The best water-splitting activity was achieved on the sample that balanced the proton conductivity and oxygen surface desorption activity through barium substitution. In the end, water-splitting resistances of 0.089 and 0.022 Ωcm^2 were reached at 600 and 700°C respectively on $Pr_{1.7}Ba_{0.3}NiO_{4+\delta}$. The corresponding full cell yielded an excellent electrolyzing current density of 0.83 A/cm^2 at 600°C, 1.96 A/cm^2 at 700°C with a 1.3V applied potential.

Acknowledgments

This investigation is funded by U.S. Department of Energy, office of Energy Efficiency and Renewable Energy (EERE) under the contract Number DE-EE0008378. We would like to thank the program managers Drs. Eric Miller and William Gibbons for the technical guidance and financial support.

References

[1] A. Scipioni, A. Manzardo, J. Ren, Hydrogen economy: supply chain, life cycle analysis and energy transition for sustainability, Academic Press, 2017.
[2] L. Zhang, X. Zhu, Z. Cao, Z. Wang, W. Li, L. Zhu, P. Li, X. Huang, Z. Lü, Pr and Ti co-doped Strontium Ferrite as a Novel Hydrogen Electrode for Solid Oxide Electrolysis Cell. Electrochim. Acta, 232, 542 (2017).
[3] J. Kim, S. Sengodan, S. Kim, O. Kwon, Y. Bu, G. Kim, Proton conducting oxides: A review of materials and applications for renewable energy conversion and storage. Renewable and Sustainable Energy Reviews, 109, 606 (2019).
[4] L. Bi, S. Boulfrad, E. Traversa, Reversible solid oxide fuel cells (R-SOFCs) with chemically stable proton-conducting oxides. Solid State Ionics, 275, 101 (2015).
[5] L. Bi, S.P. Shafi, E. Traversa, Y-doped BaZrO 3 as a chemically stable electrolyte for proton-conducting solid oxide electrolysis cells (SOECs). Journal of Materials Chemistry A, 3, 5815 (2015).
[6] L. Bi, S. Boulfrad, E. Traversa, Steam electrolysis by solid oxide electrolysis cells (SOECs) with proton-conducting oxides. Chem. Soc. Rev., 43, 8255 (2014).
[7] L. Lei, J. Zhang, Z. Yuan, J. Liu, M. Ni, F. Chen, Progress Report on Proton Conducting Solid Oxide Electrolysis Cells. Adv. Funct. Mater., 29, 1903805 (2019).
[8] E. Fabbri, L. Bi, H. Tanaka, D. Pergolesi, E. Traversa, Chemically stable Pr and Y co‐doped barium zirconate electrolytes with high proton conductivity for intermediate‐temperature solid oxide fuel cells. Advanced Functional Materials, 21, 158 (2011).
[9] J. Mergel, M. Carmo, D. Fritz, Status on technologies for hydrogen production by water electrolysis. Transition to renewable energy systems, 425 (2013).
[10] E. Fabbri, D. Pergolesi, E. Traversa, Materials challenges toward proton-conducting oxide fuel cells: a critical review. Chem. Soc. Rev., 39, 4355 (2010).
[11] W. Li, B. Guan, L. Ma, S. Hu, N. Zhang, X. Liu, High performing triple-conductive Pr2NiO4+δ anode for proton-conducting steam solid oxide electrolysis cell. Journal of Materials Chemistry A, 6, 18057 (2018).
[12] L. Lei, Z. Tao, X. Wang, J.P. Lemmon, F. Chen, Intermediate-temperature solid oxide electrolysis cells with thin proton-conducting electrolyte and a robust air electrode. Journal of Materials Chemistry A, 5, 22945 (2017).
[13] D. Huan, W. Wang, Y. Xie, N. Shi, Y. Wan, C. Xia, R. Peng, Y. Lu, Investigation of real polarization resistance for electrode performance in proton-conducting electrolysis cells. Journal of Materials Chemistry A, 6, 18508 (2018).

[14] Y. Chen, S. Yoo, K. Pei, D. Chen, L. Zhang, B. deGlee, R. Murphy, B. Zhao, Y. Zhang, Y. Chen, An In Situ Formed, Dual‐Phase Cathode with a Highly Active Catalyst Coating for Protonic Ceramic Fuel Cells. Advanced Functional Materials, 28, 1704907 (2018).
[15] X. Jiang, J. Wang, G. Jia, Z. Qie, Y. Shi, A. Idrees, Q. Zhang, L. Jiang, Characterization of PrBa0.92CoCuO6−δ as a potential cathode material of intermediate-temperature solid oxide fuel cell. Int. J. Hydrogen Energy, 42, 6281 (2017).
[16] W. Li, B. Guan, L. Ma, H. Tian, X. Liu, Synergistic Coupling of Proton-Conductors BaZr0. 1Ce0. 7Y0. 1Yb0. 1O3-δ and La2Ce2O7 to Create Chemical Stable, Interface Active Electrolyte for Steam Electrolysis Cells. ACS Applied Materials & Interfaces, (2019).
[17] W. Wu, H. Ding, Y. Zhang, Y. Ding, P. Katiyar, P.K. Majumdar, T. He, D. Ding, 3D Self-Architectured Steam Electrode Enabled Efficient and Durable Hydrogen Production in a Proton-Conducting Solid Oxide Electrolysis Cell at Temperatures Lower Than 600 °C. Advanced Science, 5, 1800360 (2018).
[18] S. Choi, T.C. Davenport, S.M. Haile, Protonic ceramic electrochemical cells for hydrogen production and electricity generation: exceptional reversibility, stability, and demonstrated faradaic efficiency. Energy & Environmental Science, 12, 206 (2019).
[19] B. Chen, H. Xu, H. Zhang, P. Tan, W. Cai, M. Ni, A novel design of solid oxide electrolyser integrated with magnesium hydride bed for hydrogen generation and storage – A dynamic simulation study. Applied Energy, 200, 260 (2017).
[20] A. Grimaud, F. Mauvy, J.M. Bassat, S. Fourcade, M. Marrony, J.C. Grenier, Hydration and transport properties of the Pr 2− x Sr x NiO 4+ δ compounds as H+-SOFC cathodes. J. Mater. Chem., 22, 16017 (2012).
[21] K. Chen, J. Hyodo, K.M. O'Donnell, W. Rickard, T. Ishihara, Effect of volatile boron species on the electrocatalytic activity of cathodes of solid oxide fuel cells: III. Ba0. 5Sr0. 5Co0. 8Fe0. 2O3-δ electrodes. J. Electrochem. Soc., 161, F1163 (2014).
[22] C. Duan, R. Kee, H. Zhu, N. Sullivan, L. Zhu, L. Bian, D. Jennings, R. O'Hayre, Highly efficient reversible protonic ceramic electrochemical cells for power generation and fuel production. Nature Energy, 4, 230 (2019).
[23] H. Ding, W. Wu, C. Jiang, Y. Ding, W. Bian, B. Hu, P. Singh, C.J. Orme, L. Wang, Y. Zhang, D. Ding, Self-sustainable protonic ceramic electrochemical cells using a triple conducting electrode for hydrogen and power production. Nature communications, 11, 1907 (2020).
[24] W. Tang, H. Ding, W. Bian, W. Wu, W. Li, X. Liu, J.Y. Gomez, C.Y. Regalado Vera, M. Zhou, D. Ding, Understanding of A-site deficiency in layered perovskites: promotion of dual reaction kinetics for water oxidation and oxygen reduction in protonic ceramic electrochemical cells. Journal of Materials Chemistry A, 8, 14600 (2020).
[25] H.-I. Yoo, S.-H. Park, J. Chun, Suppression of Electronic Conductivity of CeO2-Based Electrolytes by Electron Traps. J. Electrochem. Soc., 157, B215 (2009).
[26] B. Guan, Z. Lv, G. Wang, B. Wei, W. Li, X. Huang, A Performance Study of Solid Oxide Fuel Cells With $BaZr_{0.1}Ce_{0.7}Y_{0.2}O_3$ Electrolyte Developed by Spray‐Modified Pressing Method. Fuel Cells, 141 (2012).
[27] W. Li, B. Guan, J. Yan, N. Zhang, X. Zhang, X. Liu, Enhanced surface exchange activity and electrode performance of (La 2− 2x Sr 2x)(Ni 1− x Mn x) O 4+ δ cathode for intermediate temperature solid oxide fuel cells. J. Power Sources, 318, 178 (2016).
[28] Z. Shao, W. Zhou, Z. Zhu, Advanced synthesis of materials for intermediate-temperature solid oxide fuel cells. Prog. Mater Sci., 57, 804 (2012).

[29] T.H. Wan, M. Saccoccio, C. Chen, F. Ciucci, Influence of the Discretization Methods on the Distribution of Relaxation Times Deconvolution: Implementing Radial Basis Functions with DRTtools. Electrochim. Acta, 184, 483 (2015).
[30] A. Weber, S. Dierickx, A. Kromp, E. Ivers‐Tiffée, Sulfur poisoning of anode‐supported SOFCs under reformate operation. Fuel Cells, 13, 487 (2013).
[31] N. Shi, F. Su, D. Huan, Y. Xie, J. Lin, W. Tan, R. Peng, C. Xia, C. Chen, Y. Lu, Performance and DRT analysis of P-SOFCs fabricated using new phase inversion combined tape casting technology. Journal of Materials Chemistry A, 5, 19664 (2017).
[32] S. Li, K. Xie, Composite oxygen electrode based on LSCF and BSCF for steam electrolysis in a proton-conducting solid oxide electrolyzer. J. Electrochem. Soc., 160, F224 (2013).
[33] N. Bausá, C. Solís, R. Strandbakke, J.M. Serra, Development of composite steam electrodes for electrolyzers based on barium zirconate. Solid State Ionics, 306, 62 (2017).
[34] S. Yang, Y. Wen, J. Zhang, Y. Lu, X. Ye, Z. Wen, Electrochemical performance and stability of cobalt-free Ln1.2Sr0.8NiO4 (Ln=La and Pr) air electrodes for proton-conducting reversible solid oxide cells. Electrochim. Acta, 267, 269 (2018).
[35] D. Huan, N. Shi, L. Zhang, W. Tan, Y. Xie, W. Wang, C. Xia, R. Peng, Y. Lu, New, Efficient, and Reliable Air Electrode Material for Proton-Conducting Reversible Solid Oxide Cells. ACS Applied Materials & Interfaces, 10, 1761 (2018).
[36] N. Danilov, J. Lyagaeva, G. Vdovin, E. Pikalova, D. Medvedev, Electricity/hydrogen conversion by the means of a protonic ceramic electrolysis cell with Nd2NiO4+δ-based oxygen electrode. Energy Convers. Manage., 172, 129 (2018).
[37] A.P. Tarutin, G.K. Vdovin, D.A. Medvedev, A.A. Yaremchenko, Fluorine-containing oxygen electrodes of the nickelate family for proton-conducting electrochemical cells. Electrochim. Acta, 337, 135808 (2020).
[38] A.-M. Azad, M. Hammoud, Fine-tuning of ceramic-based chemical sensors via novel microstructural modification: I: Low level CO sensing by tungsten oxide, WO3. Sensors and Actuators B: Chemical, 119, 384 (2006).
[39] M.A. Azimova, S. McIntosh, On the reversibility of anode supported proton conducting solid oxide cells. Solid State Ionics, 203, 57 (2011).
[40] J. Lyagaeva, N. Danilov, G. Vdovin, J. Bu, D. Medvedev, A. Demin, P. Tsiakaras, A new Dy-doped BaCeO 3–BaZrO 3 proton-conducting material as a promising electrolyte for reversible solid oxide fuel cells. Journal of Materials Chemistry A, 4, 15390 (2016).
[41] S. Yang, Y. Wen, S. Zhang, S. Gu, Z. Wen, X. Ye, Performance and stability of BaCe0.8−xZr0.2InxO3−δ-based materials and reversible solid oxide cells working at intermediate temperature. Int. J. Hydrogen Energy, 42, 28549 (2017).
[42] K. Leonard, Y. Okuyama, Y. Takamura, Y.-S. Lee, K. Miyazaki, M.E. Ivanova, W.A. Meulenberg, H. Matsumoto, Efficient intermediate-temperature steam electrolysis with Y : SrZrO3–SrCeO3 and Y : BaZrO3–BaCeO3 proton conducting perovskites. Journal of Materials Chemistry A, 6, 19113 (2018).
[43] E. Vøllestad, R. Strandbakke, M. Tarach, D. Catalán-Martínez, M.-L. Fontaine, D. Beeaff, D.R. Clark, J.M. Serra, T. Norby, Mixed proton and electron conducting double perovskite anodes for stable and efficient tubular proton ceramic electrolysers. Nature materials, 18, 752 (2019).
[44] W. Wu, Y. Zhang, D. Ding, T. He, A High‐Performing Direct Carbon Fuel Cell with a 3D Architectured Anode Operated Below 600° C. Adv. Mater., 30, 1704745 (2018).

[45] F. He, M. Liang, W. Wang, R. Ran, G. Yang, W. Zhou, Z. Shao, High-Performance Proton-Conducting Fuel Cell with B-Site-Deficient Perovskites for All Cell Components. Energy & Fuels, 34, 11464 (2020).
[46] E. Dogdibegovic, Q. Cai, N.S. Alabri, W. Guan, X.-D. Zhou, Activity and Stability of (Pr1-xNdx)2NiO4as Cathodes for Solid Oxide Fuel Cells. J. Electrochem. Soc., 164, F99 (2016).
[47] A.J. Bard, L.R. Faulkner, J. Leddy, C.G. Zoski, Electrochemical methods: fundamentals and applications, Wiley New York, 1980.
[48] A. Bielański, J. Haber, Oxygen in catalysis on transition metal oxides. Catalysis Reviews Science and Engineering, 19, 1 (1979).
[49] T. Nakamura, K. Yashiro, K. Sato, J. Mizusaki, Oxygen nonstoichiometry and defect equilibrium in La 2− x Sr x NiO 4+ δ. Solid State Ionics, 180, 368 (2009).
[50] I. Yasuda, T. Hikita, Precise Determination of the Chemical Diffusion Coefficient of Calcium - Doped Lanthanum Chromites by Means of Electrical Conductivity Relaxation. J. Electrochem. Soc., 141, 1268 (1994).
[51] Y. Li, K. Gerdes, X. Liu, Oxygen Transport Kinetics in Infiltrated SOFCs Cathode by Electrical Conductivity Relaxation Technique. J. Electrochem. Soc., 160, F554 (2013).
[52] B. Guan, W. Li, X. Zhang, X. Liu, Surface Oxygen Exchange Properties of Sr Doped La2NiO4+δ as SOFC Cathode: Thin-Film Electrical Conductivity Relaxation Investigation. ECS Transactions, 68, 801 (2015).
[53] Y. Li, K. Gerdes, H. Diamond, X. Liu, An improved method to increase the predictive accuracy of the ECR technique. Solid State Ionics, 204–205, 104 (2011).
[54] M.W. den Otter, A study of oxygen transport in mixed conducting oxides using isotopic exchange and conductivity relaxation. (2000).
[55] S. Adler, J. Lane, B. Steele, Electrode Kinetics of Porous Mixed - Conducting Oxygen Electrodes. J. Electrochem. Soc., 143, 3554 (1996).
[56] S. Adler, Mechanism and kinetics of oxygen reduction on porous La< sub> 1− x</sub> Sr< sub> x</sub> CoO< sub> 3− δ</sub> electrodes. Solid State Ionics, 111, 125 (1998).
[57] W. Li, B. Guan, T. Yang, N. Zhang, X. Zhang, X. Liu, On the bulk transport process and its impact on the electrode behavior of mixed conducting electrodes for SOFCs. PCCP, 19, 23218 (2017).
[58] J. Nielsen, J. Hjelm, Impedance of SOFC electrodes: A review and a comprehensive case study on the impedance of LSM:YSZ cathodes. Electrochim. Acta, 115, 31 (2014).
[59] H. Qi, F. Xia, T. Yang, W. Li, W. Li, L. Ma, G. Collins, W. Shi, H. Tian, S. Hu, T. Thomas, E.M. Sabolsky, J. Zondlo, R. Hart, H. Finklea, G.A. Hackett, X. Liu, In Situ Exsolved Nanoparticles on La0.5Sr1.5Fe1.5Mo0.5O6-δ Anode Enhance the Hydrogen Oxidation Reaction in SOFCs. J. Electrochem. Soc., 167, 024510 (2020).
[60] B.A. Boukamp, H.J.M. Bouwmeester, A.J. Burggraaf, The surface oxygen exchange process in oxygen ion conducting materials, in: T.A. Ramanarayanan, W.L. Worrell, H.L. Tuller (Eds.) Proceedings of the 2nd International Symposium on Ionic and Mixed Conducting Ceramics, The Electrochemical Society, Pennington, NJ, 1994, pp. 141.
[61] W. Li, M. Gong, X. Liu, H2 Oxidation on Doped Yttrium Chromites/Yttrium Stabilized Zirconia Anode of Solid Oxide Fuel Cell. J. Power Sources, 241, 494 (2013).
[62] B.A. Boukamp, I.C. Vinke, K.J. De Vries, A.J. Burggraaf, Surface Oxygen Exchange Kinetics of Solid Oxide Ion Conductors, in: B. Scrosati, A. Magistris, C.M. Mari, G. Mariotto (Eds.) Fast Ion Transport in Solids, Springer Netherlands, Dordrecht, 1993, pp. 167.
[63] R. De Souza, A universal empirical expression for the isotope surface exchange coefficients (k*) of acceptor-doped perovskite and fluorite oxides. PCCP, 8, 890 (2006).

[64] J.D. Kim, G.D. Kim, J.W. Moon, Y. Park, W.H. Lee, K. Kobayashi, M. Nagai, C.E. Kim, Characterization of LSM–YSZ composite electrode by ac impedance spectroscopy. Solid State Ionics, 143, 379 (2001).
[65] A. Flura, C. Nicollet, S. Fourcade, V. Vibhu, A. Rougier, J.M. Bassat, J.C. Grenier, Identification and modelling of the oxygen gas diffusion impedance in SOFC porous electrodes: application to Pr2NiO4+δ. Electrochim. Acta, 174, 1030 (2015).
[66] W. Shi, Z. Lyu, M. Han, Distribution of Relaxation Time Analysis of the Initial Performance Degradation on Ni-YSZ Anode Support Cells. ECS Transactions, 91, 791 (2019).
[67] M.J. Jørgensen, M. Mogensen, Impedance of solid oxide fuel cell LSM/YSZ composite cathodes. Journal of the Electrochemical Society, 148, A433 (2001).
[68] J.R. Smith, A. Chen, D. Gostovic, D. Hickey, D. Kundinger, K.L. Duncan, R.T. DeHoff, K.S. Jones, E.D. Wachsman, Evaluation of the relationship between cathode microstructure and electrochemical behavior for SOFCs. Solid State Ionics, 180, 90 (2009).
[69] R. Zohourian, R. Merkle, G. Raimondi, J. Maier, Mixed ‐ conducting perovskites as cathode materials for protonic ceramic fuel cells: understanding the trends in proton uptake. Adv. Funct. Mater., 28, 1801241 (2018).
[70] D. Poetzsch, R. Merkle, J. Maier, Stoichiometry Variation in Materials with Three Mobile Carriers—Thermodynamics and Transport Kinetics Exemplified for Protons, Oxygen Vacancies, and Holes. Advanced Functional Materials, 25, 1542 (2015).